Applied Catalysis B: Environmental 237 (2018) 1091–1100

Contents lists available at ScienceDirect

Applied Catalysis B: Environmental

journal homepage: www.elsevier.com/locate/apcatb

Homogeneous and heterogeneous photocatalytic water oxidation by polyoxometalates containing the most earth-abundant transition metal, iron

Min Zheng[a], Yong Ding[a,b,*], Xiaohu Cao[a], Tian Tian[a], Junqi Lin[a]

[a] State Key Laboratory of Applied Organic Chemistry, Key Laboratory of Nonferrous Metals Chemistry and Resources Utilization of Gansu Province, and College of Chemistry and Chemical Engineering, Lanzhou University, Lanzhou 730000, China

[b] State Key Laboratory for Oxo Synthesis and Selective Oxidation, Lanzhou Institute of Chemical Physics, Chinese Academy of Sciences, Lanzhou 730000, China

ARTICLE INFO

Keywords:
Photocatalytic water oxidation
Tetrairon(III)-substituted polyoxometalate
Homogeneous catalysis
Heterogeneous catalysis
Mesoporous SBA-15

ABSTRACT

Reported here, inorganic molecular tetrairon(III)-substituted polyoxotungstate $[Fe_4^{III}(H_2O)_2(P_2W_{15}O_{56})_2]^{12-}$ is firstly used to catalyze visible-light-driven oxygen evolution, which displays excellent catalytic activity (O_2 yield of 48%, turnover number ($TON_{catalyst}$) of 900 and quantum (Φ_{QY}) yield of 24%) in a homogeneous system. The O_2 yield and TON of Fe_4POM catalyst rank third and fourth among thirty documented homogeneous photocatalytic water oxidation catalysts based on POMs, respectively. In order to recover and reuse the homogeneous catalysts, it is realistic and necessary to heterogenize the homogeneous molecular catalyst. The electrostatic interaction is rationally designed as solid connection between ((3-aminopropyl)triethoxysilane) apts-modified mesoporous SBA-15 and polyoxoanion (Fe_4POM). The catalytically active species of immobilized polyoxometalate maintains intact before and after the photocatalytic water oxidation, which is adequately confirmed by various spectroscopic techniques such as solid phosphorus-31 nuclear magnetic resonance spectra (^{31}P MAS NMR), X-ray photoelectron spectra (XPS) and transmission electron microscopy (TEM) images.

1. Introduction

As the largest exploitable resource, the incidence of solar energy (at the power level of 1 kW m^{-2} on the surface of earth) to the earth in one hour exceeds all human energy consumption in one year [1–3]. Visible-light-driven water splitting under artificial photosynthesis system provides an interesting novel insight in the sustainable and clean hydrogen energy to replace those non-renewable fossil resources (including coal, oil and natural gas) [4–8]. However, since a large positive change in Gibbs energy ($\Delta G = 237\ kJ\ mol^{-1} > 0$) exists in the conversion of photon energy to chemical energy through water splitting, this "up-hill" reaction requires effective photocatalysts to improve its thermodynamically unfavorable property [9–13]. To further figure out the bottleneck problems, exploring robust water oxidation catalyst (WOC) to promote the sluggish kinetic of complicated four electrons process is becoming the increasingly focused issue among overall water splitting [14–16].

With highly hydrolytic and oxidative stability, all-inorganic materials of early transition metal-oxygen anion clusters or polyoxometalates (POMs) were used as robust WOC [17–22]. The oligomeric aggregate formed by self-assembly process is essential advantageous character of POMs, in which empty d-orbitals metal cations (mostly the d° early transition metal Mo(VI), W(VI), V(V), Nb(V) and Ta(V)) are accessibly bridged by oxide anions (corner-shared, edge-shared, coplanar occasionally) for forming metal-oxygen bonding [23,24]. Another fascinating feature of POMs is the metal substitution property, which means the framework d° species could be replaced by d- or p-block ions through rational synthetic methods. The d-electron transition-metal-substituted polyoxometalate (TMSP) relatives are sufficient to supply catalytic active metal sites, and maintain the multidentate morphology to fulfill oxidatively resistant function with totally inorganic ligands at the same time [25]. Thus, polyoxoanions are promising catalysts for photocatalytic water oxidation due to its principal properties and encouraging potentials [26–30], especially based on the most abundant and inexpensive transition metal elements, iron [31].

Herein, we report that a molecular tetrairon(III)-substituted polyoxotungstate $[Fe_4^{III}(H_2O)_2(P_2W_{15}O_{56})_2]^{12-}$ was firstly used to catalyze visible-light-driven oxygen evolution, which illustrated good catalytic activity in homogeneous system with O_2 yield of 48%, $TOF_{catalyst}$ of 5 s^{-1} and Φ_{QY} yield of 24%. The O_2 yield and TON of Fe_4POM catalyst rank third and fourth among thirty documented homogeneous photocatalytic water oxidation catalysts based on POMs, respectively.

* Corresponding author at: State Key Laboratory of Applied Organic Chemistry, Key Laboratory of Nonferrous Metals Chemistry and Resources Utilization of Gansu Province, and College of Chemistry and Chemical Engineering, Lanzhou University, Lanzhou 730000, China.
E-mail addresses: dingyong1@lzu.edu.cn, dingyong1973@163.com (Y. Ding).

https://doi.org/10.1016/j.apcatb.2018.07.014
Received 11 June 2018; Received in revised form 29 June 2018; Accepted 4 July 2018
Available online 05 July 2018

However, since almost all POMs with good oxygen evolution ability are completely soluble in water oxidation reaction conditions, the homogeneous catalysts are difficult to recover and recycle. Heterogeneous catalysts are reusable because they can be easily separated from reaction system. Therefore, it is realistic and necessary to heterogenize the homogeneous molecular catalyst.

In order to reuse the catalyst and further analyze the catalytic active species during photocatalytic water oxidation, the robust tetrairon(III)-containing Fe_4POM was anchored on SBA-15 by electrostatic interaction. Before immobilization, the surface of mesoporous molecular sieve was modified with (3-aminopropyl)triethoxysilane (apts) to form ammonium cations under acid condition. The structure of immobilized polyoxoanion remained intact during this cation exchange process and kept comparable activity for oxygen evolution in heterogeneous system, which was subsequently confirmed by various spectroscopic techniques in this paper. The heterogenization of homogeneous catalysis is forecasted to be the industrialization tendency for water splitting (including the half reaction of water oxidation). Besides, building the close relationship between homogeneous and heterogeneous process is an elegant way to efficiently bridge the gap between these two traditional disciplines.

2. Experiment section

2.1. Preparation of α,β-$K_6P_2W_{18}O_{62}$

Na_2WO_4-$2H_2O$ (30 g) was added to 105 mL of water, and the solution was heated to boiling. Then 45 mL of 85% H_3PO_4 was slowly added to the boiling solution, and the resulting yellow-green solution was refluxed for 8 h. The solution was cooled, and the product was precipitated by addition of 30 g of solid KCl. The light green precipitate was collected, redissolved in a minimum amount of hot water, and allowed to crystallize at 5 °C overnight. A typical yield was 21 g after drying at 80 °C under vacuum for several hours. The $K_6P_2W_{18}O_{62}$ prepared this way is always a mixture of α and β isomers (ca. 90–95% α form) identified by ^{31}P NMR (α, −12.7 ppm; β, −11 and −11.6 ppm).

2.2. Preparation of α-$K_6P_2W_{18}O_{62}$

About 21 g of the α,β-$K_6P_2W_{18}O_{62}$ mixture was dissolved in 75 mL of water, contained in a 500-mL flask and then heated. A drop of bromine was added to the warm solution, causing the green solution to turn bright yellow by oxidizing any reduced polyoxoanion. The solution was then cooled to room temperature. A 10% $KHCO_3$ solution was slowly poured into the stirring P_2W_{18} solution. After addition of ca. 75 mL of $KHCO_3$, the solution became cloudy and the white salt $K_{10}P_2W_{17}O_{61}$ precipitated. The $KHCO_3$ addition was continued until the solution was colorless and no more salt formed (approximately 120 mL more $KHCO_3$ was needed to reach this point). About 33 mL of 6 M HCl was carefully added to the P_2W_{17} mixture, regenerating a clear yellow solution of α-P_2W_{18}. This solution was then boiled for 1 h, reducing the volume to ca. 300 mL. Any insoluble material was removed by hot filtration. Solid KCl (30 g) was added to the hot solution, and the mixture was cooled at 5 °C overnight. A typical yield was 15–18 g (70–85% recovery) of the yellow crystalline salt, α-$K_6P_2W_{18}O_{62}$.

2.3. Preparation of $Na_{12}P_2W_{15}O_{56}{\cdot}18H_2O$ [32,33]

The salt α-$K_6P_2W_{18}O_{62}$ (10.0 g; the pure α salt unless indicated otherwise) was dissolved in 25 mL of H_2O with moderate heating. After the solution had cooled to room temperature, 7.5 g of $NaClO_4$ was added. A white precipitate of $KClO_4$ formed immediately, then the mixture was stirred for 1 h. $KClO_4$ was removed by filtration. Na_2CO_3 (1 M) was added dropwise to the filtrate. At pH 8.5, a white precipitate began to form. More base was added until pH 9, and this pH was maintained by intermittent base addition for 1 h. The solid $Na_{12}P_2W_{15}O_{56}$ was collected and washed with 37.5 mL of a saturated NaCl solution, 37.5 mL of 95% ethanol, and 37.5 mL of diethyl ether. The solid was dried in a desiccator over concentrated H_2SO_4 for 2 days. A yield was 7.6 g of a white solid (85%). Drying for longer times resulted in a hygroscopic product.

2.4. Synthesis of $H_5Na_7[Fe^{III}_4(H_2O)_2(P_2W_{15}O_{56})_2]{\cdot}48H_2O$ (H_5Na_7-Fe_4POM) and $Na_{12}[Fe^{III}_4(H_2O)_2(P_2W_{15}O_{56})_2]{\cdot}58H_2O$ (Na_{12}-Fe_4POM)

The polymeric complex, H_5Na_7-Fe_4POM, was prepared as follows. To a solution of 0.82 g (3 mmol) of $FeCl_3{\cdot}6H_2O$ in 40 mL of H_2O was added slowly with vigorous stirring 6.0 g (1.5 mmol) of $Na_{12}P_2W_{15}O_{56}{\cdot}18H_2O$. The solution was heated at 80 °C until the volume was reduced to ~22 mL. NaCl (1.5 g, 26 mmol) was added. The solution was filtered hot and the supernatant left unstirred in a beaker open to the air. After several days, orange columnar crystals formed (1.8 g, 30% yield). The complex with the monomeric motif, Na_{12}-Fe_4POM, was prepared by a slightly different procedure as follows. To a solution of 0.82 g (3 mmol) of $FeCl_3{\cdot}6H_2O$ in 30 mL of 2 M NaCl solution was added slowly with vigorous stirring 6.0 g (1.5 mmol) of $Na_{12}P_2W_{15}O_{56}{\cdot}18H_2O$. The solution was heated to 80 °C for 5 min and filtered hot. The filtrate was left in the air. After several days, a yellow crystalline solid formed (1.8 g, 30% yield). The needle-shaped crystals of Na_{12}-Fe_4POM were dichroic: yellow along the short axis and brown along the long axis.

2.5. Preparation of pure silica SBA-15

Pure siliceous SBA-15 was prepared as previously described [34]. In a typical run, 8.0 g of Pluronic P123 was dissolved in 60 g of deionized water and 240 g of 2 mol L^{-1} HCl solution with stirring at 308 K. This solution was added with 17 g of tetraethoxysilane (TEOS) with stirring at 308 K for 24 h, transferred to a Teflon bottle, and then aged at 353 K for 24 h without stirring. The solid product was recovered, washed, and then air-dried at room temperature. The obtained materials were calcined in air at 773 K for 6 h with a heating rate of 1 K min^{-1} from room temperature to remove the template and then stored before use.

2.6. Preparation of iron(III)-substituted polyoxotungstates immobilized on SBA-15 [35]

Briefly, 1 g of mesoporous silica SBA-15 was heated to 130 °C for 5 h in vacuum to remove the adsorbed water. Then, under a Ar atmosphere, 30 mL of a 3 wt % solution of (3-aminopropyl)triethoxysilane (apts) in anhydrous toluene was added to the silica. After refluxing for 5 h, the solids were filtered and washed with toluene to remove unanchored apts. The solids were collected and dried for the condensation process to obtain the amino group modified silica. To immobilize Fe_4POM, 0.5 g of the modified silica was mixed with 100 mL of water, and HCl (2 M) was added to adjust the pH to about 2. Then, 0.1 g of Fe_4POM was added, and the mixture was stirred for 8 h. The solids were filtered and washed with water and then dried.

2.7. Characterization

Crystalline structures were determined by X-ray diffraction (XRD) using a Rigaku D/MAX 2400 diffractometer (Japan) with Cu Kα radiation (λ = 1.5418 Å) operating at 40 kV and 40 mA in the 2θ range of 0°–5°. X-ray photoelectron spectroscopy (XPS) spectra were measured by ESCALAB250xi with X-ray monochromatisation. The binding energy of each element was corrected by C 1s peak (284.8 eV) from residual carbon. UV–vis absorption spectra were recorded on Beijing Purkinje General Instrument Co., Ltd. TU-1810 spectrophotometer equipped with a photomutiplier tube detector. Infrared spectra (2–4 wt% sample in KBr pellets) were recorded using a Bruker VERTEX 70v FT-IR spectrometer. The liquid ^{31}P NMR spectra were measured using a Bruker

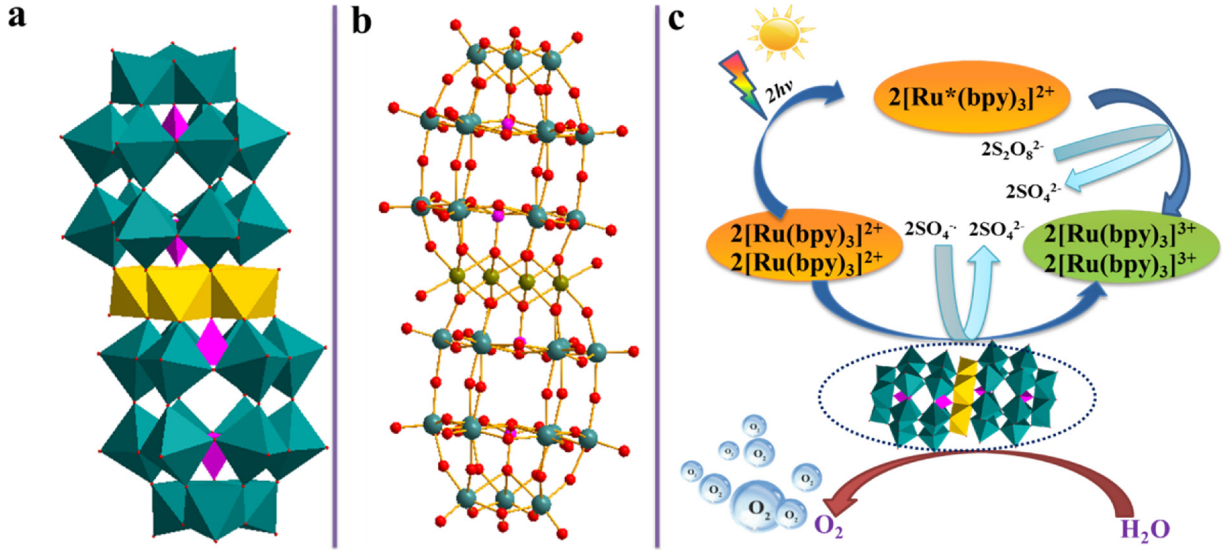

Fig. 1. (a) Polyhedral and (b) ball-and-stick representation of Fe_4POM. Color scheme: $[Fe_4^{III}O_{14}(H_2O)_2]$ polyhedra (yellow); Fe (cyan), W (dark blue), O (red). (c) The photocatalytic water oxidation cycle in the presence of catalyst, photosensitizer and electron acceptor.

400 MHz spectrometer in D_2O with tetramethylsilane $[Si(CH_3)_4]$ as an internal standard. Internal reference of 85% H_3PO_4 was recorded in a sealed capillary centered in a 12-mm sample tube. Chemical shifts upfield of H_3PO_4 are reported as negative values. The solid ^{31}P MAS NMR spectra spectra were collected with a Bruker Avance III 400 MHz NMR spectrometer using 4 mm solid nuclear magnetic probe. The GC–MS spectral analysis was used to detect the produced oxygen. The O_2 in the sampled gas was separated by passing through a 2 m × 3 mm packed molecular sieve 5 Å column with an Ar carrier gas and quantified by a thermal conductivity detector (TCD) (Shimadzu GC-9A). Transmission electron microscopy (TEM) images were collected with a JEOL JEM-2010 instrument operating at 200 kV. Nanosecond transient absorption measurements were performed on an Edinburgh Instruments LP920-KS laser flash photolysis spectrometer, using an OPO laser source (OPOTEK Vibrant). Transient detection was obtained using a photomultiplieroscilloscope combination (Hamamatsu R928P, Tektronix TDS3012C). Kinetics of bleach recovery conditions: Excitation wavelength = 445 nm, analysis wavelength = 450 nm.

2.8. Calculations

(1). The quantum yield (Φ_{QY}) of O_2 evolution:

$$\Phi_{QY(initial)} = 2 \times \frac{\text{initial O}_2\text{ formation rate}}{\text{photon flux}} \times 100\%$$

(2). The oxygen yield of O_2 evolution:

$$O_2 \text{ yield} = 2 \times \frac{\text{mole of O}_2\text{ evolution}}{\text{mole of Na}_2S_2O_8} \times 100\%$$

(3). The turnover number (TON) of O_2 evolution:

$$TON_{catalyst} = \frac{\text{mole of O}_2\text{ evolution}}{\text{mole of catalyst}} \times 100\%$$

(4). The turnover frequency (TOF) of O_2 evolution:

$$TOF_{catalyst} = \frac{\text{mole of oxygen produced in 1 min}}{60\text{ s} \times \text{mole of catalyst}} \times 100\%$$

3. Results and discussion

3.1. Homogeneous system

The tetrairon(III)-substituted Fe_4POM ($[Fe_4^{III}(H_2O)_2(P_2W_{15}O_{56})_2]^{12-}$) was prepared according to procedure reported firstly by Craig L. Hill and co-workers in 1997 [36], which is a modified method for the formula $[(TM)_4^{II}(H_2O)_2(P_2W_{15}O_{56})_2]^{16-}$ (TM = one first-row transition metal cations) with sandwich complexes [32]. After merging trivacant heteropolytungstate α-$[P_2W_{15}O_{56}]^{12-}$ and aqueous Fe^{3+} together, two ferric polytungstophosphate derivatives were obtained to further form the Wells-Dawson-derived

TMSP sandwiched structure. Two different cationic kinds of iron-containing POMs were prepared and isolated separately, and both of them exhibit identical properties in water oxidation system since anions of heteropolytungstate remain the same in aqueous solution. Stacked needles of Na_{12}-Fe_4POM were obtained at higher sodium chloride concentration of 2 M (pH ≈ 3), in which each polyanion is well separated by the sodium cations. While elongated prisms (column-shaped) of H_5Na_7-Fe_4POM was achieved by adjusting the sodium chloride concentration to 1 M (pH ≈ 1), and the one-dimensional polymeric array formed due to polyanion linked by ion pairing with forcefully associated hydrated sodium cations. The identical features of this two iron-containing POMs with different cations are verified by Fourier transform infrared (FT-IR) in Fig. S1. Since the main purpose of this work is focused on the water oxidation performance of heteropoly anions in the homogeneous aqueous solution, only polyanions (Fe_4POM) are thoroughly investigated in the following content.

Single-crystal X-ray diffraction structural data was summarized in Table S1. Two trivacant Wells-Dawson portions (α-$[P_2W_{15}O_{56}]^{12-}$) are dimeric together via the oxo-aqua tetranuclear iron core ($[Fe_4^{III}O_{14}(H_2O)_2]$) and then form the sandwiched structure of polyanion Fe_4POM (Fig. 1). The crystallographic data and structural refinements of Fe_4POM illustrate that the polyanion consists of C_{2h} symmetry and approximate axial from P1 to P2. The four edge-shared octahedras (FeO_6) in the center look like a rhombus, and each vertex occupied by oxo groups on both faces of the rhombus is corner-shared with two α-$[P_2W_{15}O_{56}]$ units. The XPS spectra were curried out to verify the valence of iron in Fe_4POM (Fig. S2). Since Fe $2p_{1/2}$ has degeneracy of two states while Fe $2p_{3/2}$ has four states in spin–orbit (j–j) coupling, major peak for Fe $2p_{3/2}$ (binding energy located at 711.0 eV) is narrower and stronger in comparison with that of Fe $2p_{1/2}$ peak (binding energy

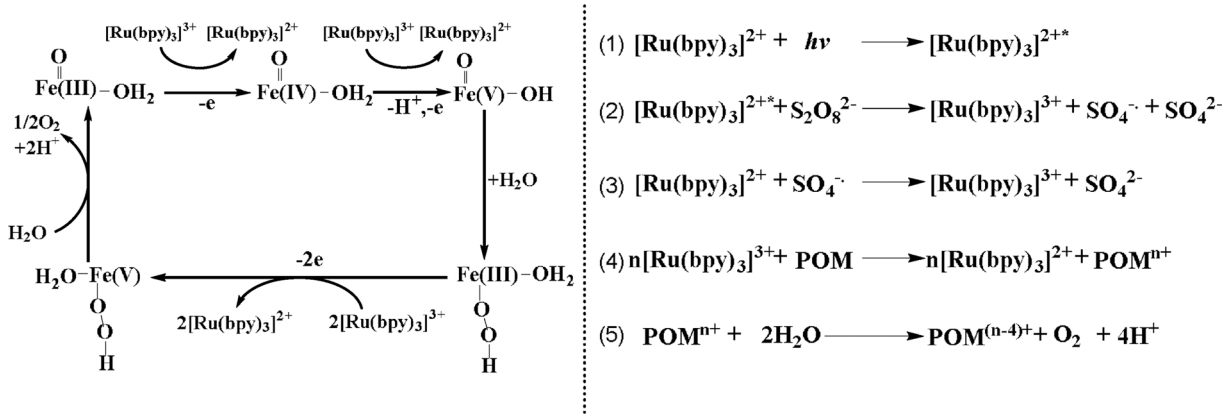

Scheme 1. The proposed four-electron catalytic mechanism of Fe_4POM in photocatalytic water oxidation cycle.

located at 724.5 eV) [37–39]. The corresponding satellite peaks result from charge transfer screening are located at around 730.1 and 717.9 eV [40], which do not overlap with two main peaks. A combination of bond valence sum (BVS) calculations and Fe 2p XPS analysis indicate that all four iron atoms in Fe_4POM are in +3 oxidation state. The four-electron catalytic mechanism of Fe_4POM in photocatalytic water oxidation is proposed in Scheme 1, in which the high-valence iron intermediates are important role for enhanced oxygen evolution.

Photocatalytic water oxidation performance with soluble Fe_4POM as homogeneous catalyst was evaluated under visible-light illumination. All O_2 evolution curves reach a platform (Fig. 2b), which could be ascribed to the exhausted sacrificial electron acceptor of $Na_2S_2O_8$ and partially decomposed photosensitizer of $[Ru(bpy)_3]Cl_2$ during photocatalytic water oxidation process [41,42]. The catalyst tetrairon(III)-substituted Fe_4POM shows fairly higher catalytic activity compared with the same equivalent moles of $FeCl_3$ (in Fig. S3). After optimizing the reaction condition, the oxygen evolution yield of 48%, $TOF_{catalyst}$ of 5 s^{-1}, $TON_{catalyst}$ of 900 and Φ_{QY} yield of 24% over catalyst Fe_4POM are obtained. From the activity comparison of O_2 yield and TON for photocatalytic water oxidation catalyzed by various documented POMs in Table S2, we can see that O_2 yield and TON of Fe_4POM rank third and fourth among thirty documented homogeneous photocatalytic water oxidation catalysts based on POMs, respectively. Therefore, the catalyst of Fe_4POM could be selected as effective photocatalyst in water oxidation reaction.

The transition character involving orbitals with both polyoxometalate ligand and central ion was monitored by UV–vis spectrum [43]. Since the intense oxygen-to-metal-charge-transfer (OMCT) bands of all d° polyoxometalates in the UV region dominate the electronic absorption spectrum, no obvious maxima for the Fe centered d-d bands in the visible region was detected. Only a subtle band around 480 nm (enlarged in the inset of Fig. 3c) of tetrairon(III)-substituted polyoxometalate in 80 mM borate buffer could be attributed to the feature of homogeneous catalyst Fe_4POM. The different UV–vis spectra curves remain nearly the identical absorbance as prolonging time to 100 min, revealing the hydrolytic stability of tetrairon(III)-substituted Fe_4POM. To further evaluate the stability of catalyst Fe_4POM in oxidized environment, the UV–vis spectra were carried out using 5 mM $Na_2S_2O_8$ in 80 mm borate buffer. The result in Fig. 3d illustrates that nearly no change was detected after a 24 h course of aging, demonstrating the stability of homogeneous catalyst Fe_4POM is not affected under the photocatalytic water oxidation medium. Besides, to get deep into exploration of structure stability, it's much more accurate to use ^{31}P NMR spectra characterization to analyze Fe_4POM catalyst (Fig. 4). Of the tetrairon(III)-substituted Fe_4POM, only one feature signal at -11.6 ppm is observed clearly in the ^{31}P NMR spectrum as the atom for P distal to the $[Fe_4^{III}O_{14}(H_2O)_2]$ unit. The ^{31}P NMR spectra were recorded at 400 MHz (Bruker Avance III NMR spectrometer), and sample Fe_4POM was prepared at typical concentration of 0.01 M by dissolving it in 80 mM borate buffers (pH 9.0) with 30% added D_2O. The 85% H_3PO_4

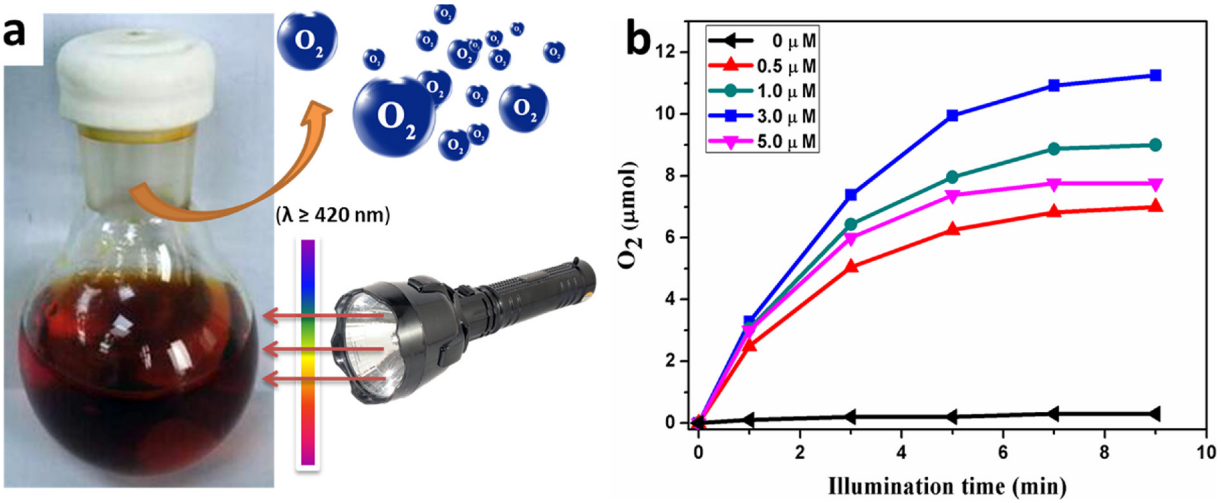

Fig. 2. (a) The experimental setup used to photocatalytic oxygen evolution. (b) The kinetics of O_2 evolution in the photocatalytic system at different concentrations of Fe_4POM. Conditions: 16 mW LED lamp equipped with a cut off filter (λ ≥ 420 nm); total reaction volume is 10 mL and overall volume is ~23.3 mL; catalyst concentration (0–5.0 μM), 1.0 mM $[Ru(bpy)_3]Cl_2$, 5.0 mM $Na_2S_2O_8$, 80 mM sodium borate buffer (initial pH 9.0); vigorous agitation using a magnetic stirrer.

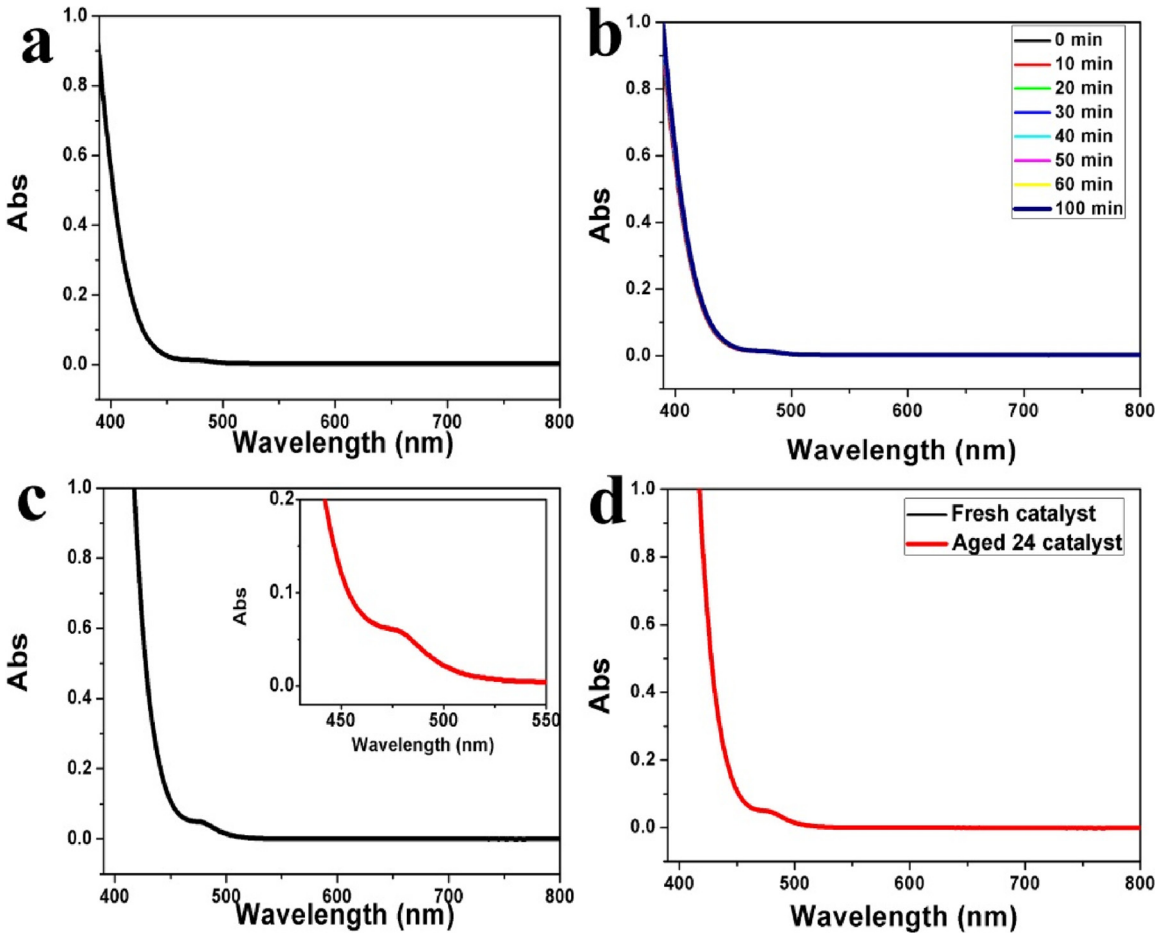

Fig. 3. UV–vis spectra of 0.5 mM Fe_4POM in H_2O (a) and corresponding aging experiment within 100 min (b), 1.0 mM Fe_4POM in 80 mM sodium borate buffer solution at pH 9.0 (c) and corresponding aging experiment in 80 mM sodium borate buffer solution at pH 9.0 with 5 mM $Na_2S_2O_8$ (d).

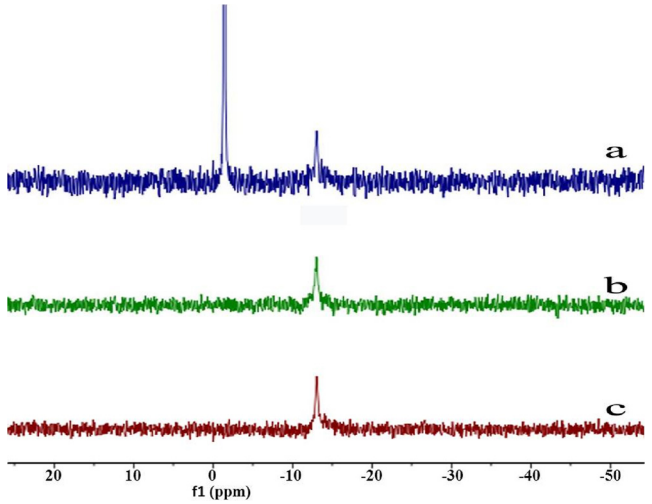

Fig. 4. ^{31}P NMR spectra of (a) internal reference of 85% H_3PO_4 was recorded in a sealed capillary centered in a 12-mm sample tube. The chemical shifts of Fe_4POM were obtained before (b) and after the reaction (c) of photocatalytic water oxidation. Samples were prepared at typical catalyst concentration of 0.01 M by dissolving in 80 mM borate buffers (pH 9.0) with 30% added D_2O.

was used as reference and it was sealed in a capillary centered in a 12-mm NMR sample tube. The chemical shifts of Fe_4POM are maintained at the same position (−11.6 ppm) before and after the photocatalytic water oxidation reaction, suggesting the tetrairon(III)-substituted Fe_4POM keeps the identical structure during photocatalytic reaction.

Laser flash photolysis [44–46] was carried out to confirm four-electron catalytic mechanism of Fe_4POM. The electron could transfer effectively from catalyst Fe_4POM to photogenerated$[Ru(bpy)_3]^{3+}$, and then high-valence intermediates generated in situ ultimately trigger water oxidation. The solution containing $[Ru(bpy)_3]^{2+}$ and $Na_2S_2O_8$ was irradiated by visible light to produce oxidized $[Ru(bpy)_3]^{3+}$ (Fig. 1c and Scheme 1). The in situ photogenerated $[Ru(bpy)_3]^{3+}$ is stepwise reduced by different concentrations of catalyst, illustrating obvious quenching of $[Ru(bpy)_3]^{3+}$ in the transient absorption experiments (Fig. S4) by detecting the absorption at 450 nm (the metal-to-ligand charge transfer (MLCT) band of $[Ru(bpy)_3]^{2+}$). With the increase of catalyst concentration, the hole-scavenging activity is increased. The $[Ru(bpy)_3]^{2+}$ is largely recovered and the oxidized catalyst is generated, which can efficiently promote water oxidation. Besides, the highest occupied molecular orbital (HOMO) in polyoxometalate is similar to the valence band in semiconductors, and the lowest unoccupied molecular orbital (LUMO) of POM could be regarded as the conduction band [47,48]. The potential difference ($\triangle E$ = HOMO($[Ru(bpy)_3]^{3+}$) − HOMO(POM)) [49] indicates that the generated photosensitizer ($[Ru(bpy)_3]^{3+}$) can oxidize Fe_4POM molecular catalyst (Figs. S6–S9), so this reaction is thermodynamically capable of promoting water oxidation.

Owing to the advantages of chemical modification and mechanistic understanding of homogeneous system, systematic improvement of catalytic ability of molecular catalyst is relatively easy compared to heterogeneous WOC. However, the homogeneous catalysts are difficult to recover and recycle since almost all POMs with good oxygen evolution ability are completely soluble in water oxidation reaction

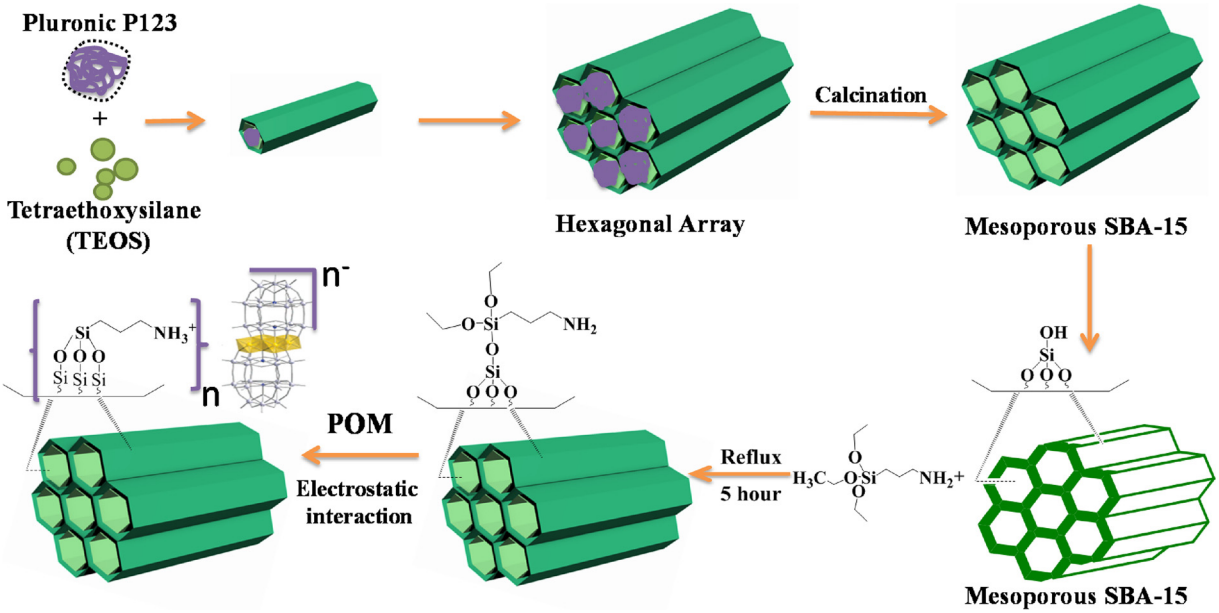

Scheme 2. The process for synthesis of pure SBA-15, modification SBA-15 and construction SBA-15-apts-Fe_4POM composite by electrostatic interaction.

conditions. Therefore, heterogenization of the homogeneous molecular catalyst is realistic and necessary.

3.2. Heterogeneous system

Mesoporous SBA-15 basement material was synthesized according to literature reported by Dongyuan Zhao et al. in 1998 [34]. This mesoporous material can be modified with ammonium cations on the surface for the sake of anchoring homogeneous molecule by electrostatic interaction [35,50]. As depicted in Scheme 2, tetraethyloxysilane (TEOS), amphiphilic triblock copolymer $EO_{20}PO_{70}EO_{20}$ (Pluronic P123) and (3-aminopropyl)triethoxysilane (apts) were used as the silicon source, template–directed

reagent and surface modified agent (silylating agent), respectively. Before immobilization, the cation was built on the surface of mesoporous molecular sieve under acid conditions. Thus, the homogeneous tetrairon(III)-containing Fe_4POM is readily immobilized onto the surface of SBA-15 by straightforward cation exchange.

As seen in Fig. 5a, a strong and sharp absorption peak at around 1063 cm^{-1} is attributed to O—Si—O antisymmetric stretching vibration, definitely confirming the silicon-oxygen tetrahedral framework in mesostructure of SBA-15 [51]. The IR band at 964 cm^{-1} and 804 cm^{-1} can be ascribed to Si—O stretching vibration and Si—O bending vibration, respectively, consistent with maintenance of the SBA-15 structure after POM immobilization. The linking ammonium cations could be detected by the band around 3300 cm^{-1} and 1500 cm^{-1} regarding as the N—H stretching vibration and N—H bending vibration [52], along with the band around 1400 cm^{-1} considered as C—N stretching vibration. To confirm the integrity of anchored polyoxotungstate, the W=O and W—O—W stretching vibrations in heterogenization were detected the same as that of homogeneous material, further revealing the catalyst Fe_4POM keeps intact after loading. Among all three samples, the broad band around 3500 cm^{-1} and weak band at approximately 1632 cm^{-1} are attributed to surface absorption —OH stretching vibration and bending vibration, respectively.

For the composite, FT-IR spectra indicate that the two-dimensional hexagonal mesostructure SBA-15 in the bulk phase is maintained, while the XPS spectra more informatively probe the surface anchored polyoxometalates [53]. Compared with pure Fe_4POM, the sample of heterogenization composite changes a lot in O 1s, Na 1s, N 1s and Si 2p spectra (Fig. 6). The disappearance of the Na 1s signal and appearance of N 1s and Si 2p signals argue strongly that cation exchange of sodium

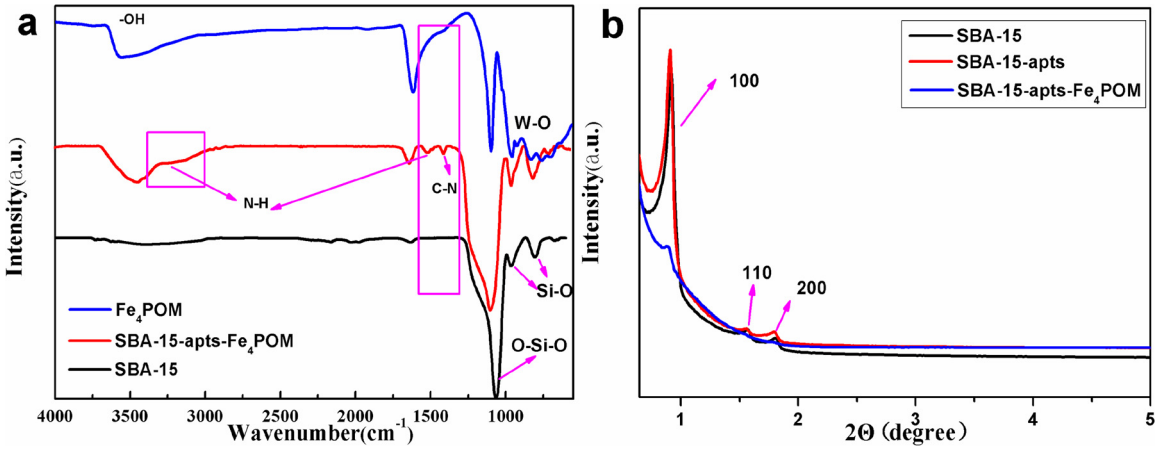

Fig. 5. (a) FT-IR spectra of Fe_4POM (blue), SBA-15 (black) and SBA-15-apts-Fe_4POM (red). (b) PXRD spectra of SBA-15 (black), SBA-15-apts (red), SBA-15-apts-Fe_4POM (blue).

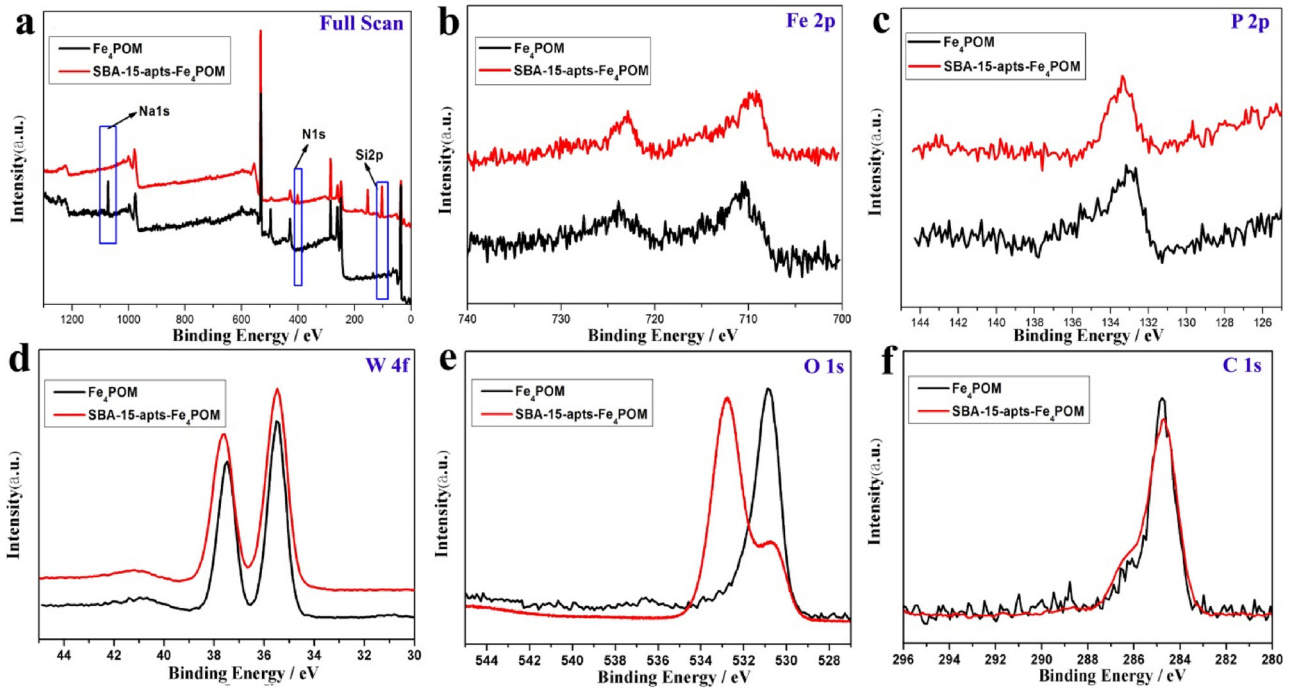

Fig. 6. XPS spectra of Fe_4POM and SBA-15-apts-Fe_4POM in the energy regions of (a) full scan, (b) Fe 2p, (c) P 2p, (d) W 4f, (e) O 1s and (d) C 1s. The binding energy position of each sample was calibrated by the C 1s peak at 284.8 eV.

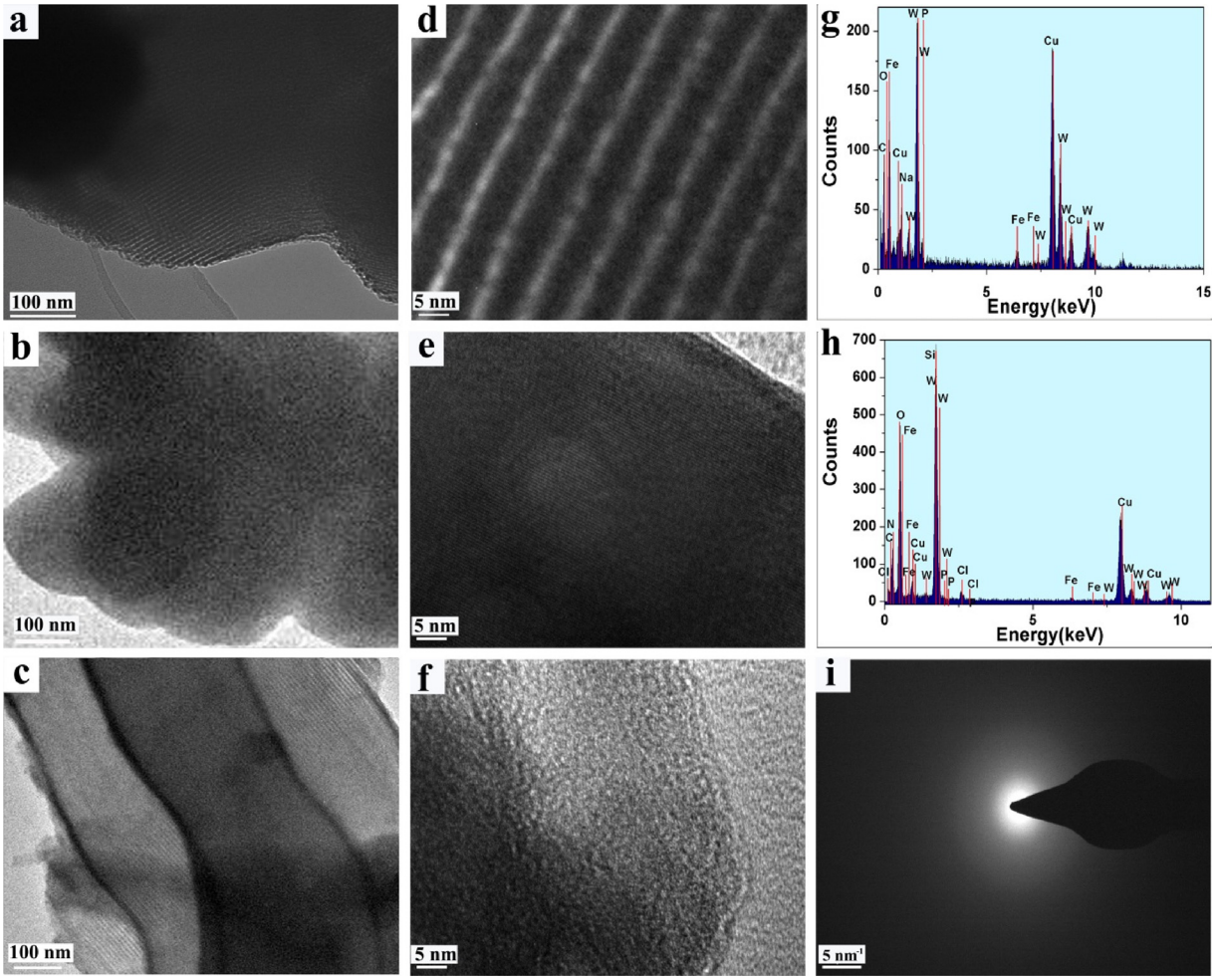

Fig. 7. TEM images of (a) SBA-15, (b) Fe_4POM (c) SBA-15-apts-Fe_4POM; HRTEM images of (d) SBA-15, (e) Fe_4POM (f) SBA-15-apts-Fe_4POM; EDX spectra of (g) Fe_4POM, (h) SBA-15-apts-Fe_4POM; SAED patterns of (i) SBA-15-apts-Fe_4POM. Scale bars, 100 nm in parts a–c; 5 nm in parts d–f.

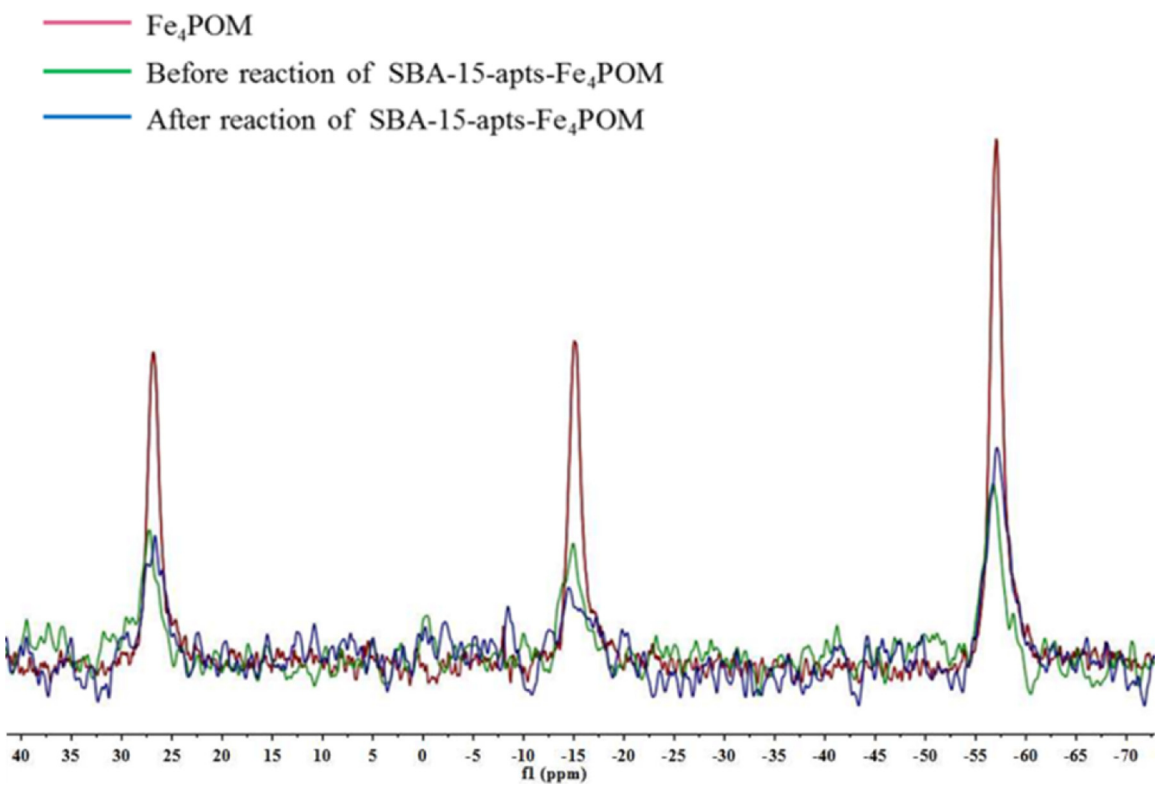

Fig. 8. Solid ^{31}P MAS NMR spectra were recorded for (red) the chemical shifts of Fe_4POM before immobilization, (green) the chemical shifts of SBA-15-apts-Fe_4POM before photocatalytic water oxidation, and (blue) the chemical shifts of SBA-15-apts-Fe_4POM after photocatalytic water oxidation.

for ammonium cations takes place. The binding energy range of 529.0–530.0 eV could be ascribed to lattice oxygen, whereas the hydroxides adsorption peak should be located at binding energy of 531.0–532.0 eV and those of H_2O adsorption peak would locate at much higher binding energy [54,55]. According to the spectra of O 1s in Fig. 6e, the proportion of lattice oxygen and oxygen adsorption toward different materials exhibits distinct difference. A larger ratio of adsorbed oxygen is observed in SBA-15-apts-Fe_4POM sample due to the existence amounts of hydroxides adsorption on the surface of mesoporous SBA-15 compared to that of pure Fe_4POM. The nearly no perturbations of the Fe 2p, P 2p and W 4f spectra at the same binding energy of polyoxometalate on the surface of mesostructure, again, argues strongly that the Fe_4POM structure maintained.

Finally, quantification of the correct ratios of Fe, P and W in Fe_4POM after immobilization by inductively coupled plasma mass spectrometry (ICP-MS) confirms the intact $[Fe^{III}_4(H_2O)_2(P_2W_{15}O_{56})_2]^{12-}$ polyoxoanion. The mass percent of Fe, P and W in the composite are 0.28%, 0.15% and 6.8%, respectively, while the calculated mole ratios are 2:2:15. After heterogenization, the loading mass percentage of intact Fe_4POM in the SBA-15-apts-Fe_4POM composite by ICP-MS analysis was approximately 10.89%. Inductively coupled plasma atomic emission spectroscopy (ICP-AES) was also used: Fe is ca. 0.30% mass percent, again consistent with the conclusion that SBA-15-apts-Fe_4POM has ~11.7% polyoxometalate.

Well-ordered hexagonal mesoporous pure SBA-15 and apts-modified SBA-15 were identified by small-angle X-ray diffraction (SXRD) (2-Theta ranges from 0 to 5 degrees in Fig. 5b). A highly intense diffraction peak at $2\theta \approx 1.0^\circ$ can be indexed to (100) lattice plane in mesoporous SBA-15, while two weak-intensity diffraction peaks that emerge at 1.7° and 1.9° are assigned to the (110) and (200) lattice planes. However, compared to pure SBA-15 and the apts-modified SBA-15 with highly ordered *p6mm* hexagonal structure, SBA-15-apts-Fe_4POM displays the reduced X-ray diffraction signal intensity. The reduced scattering intensity of the mesoporous silica provides evidence that grafting Fe_4POM was successfully achieved on the surface of framework [56,57]. The dramatic intensity decline of (100) lattice plane diffraction peak along with almost disappeared diffraction peaks of (110) and (200) lattice plane can be ascribed to the surface immobilization of Fe_4POM. TEM further confirmed the successful immobilization of the Fe_4POM polyanion on the surface of SBA-15, revealing the well-ordered *p6mm* hexagonal structure of SBA-15-apts-Fe_4POM.

The TEM and high-resolution transmission electron microscopy (HRTEM) images of pure silica (SBA-15) show the highly ordered hexagonal mesoporous structure (Fig. 7a and d). However, the lattice fringes characterization of Fe_4POM could be observed only in HRTEM (Fig. 7e), while it looks like a mass of black in the horizon for TEM analysis (Fig. 7b). After anchoring the polyoxometalates on the surface of mesoporous SBA-15, the well-distributed Fe_4POM is observed as uniformly dispersed black domains on the mesoporous material (Fig. 7c). In the SBA-15-apts-Fe_4POM composite, the SBA-15 framework keeps the well-ordered mesostructure after loading of the polyoxometalate on the pore surfaces. The obvious decrease of apparent ordered regularity in composite SBA-15-apts-Fe_4POM is found by comparison with the lattice fringe structure in pure SBA-15 (Fig. 7d, f). The selected-area electron diffraction (SAED) pattern further confirms the amorphous phase of composite material by obvious observation of diffused ring in electron diffraction spectrum. The framework of apts-modified mesoporous SBA-15 could be ascertained as the emergence of Si and N elements in the EDX spectrum (Fig. 7h) and the appearance of Cl element is ascribed to the acid condition (using HCl) for forming ammonia cations. At the same time, the molar ratio of Fe, P, W form EDX is essentially the same in pure Fe_4POM and in the SBA-15-apts-Fe_4POM composite, demonstrating the structure of homogeneous catalyst maintain intact before and after heterogenization.

The solid-state (MAS) ^{31}P NMR spectra were carried out as an unambiguous method to identify the intact structure of Fe_4POM (Fig. 8). The solid immobilization of tetrairon(III)-substituted Fe_4POM on the surface of the SBA-15 is certificated by the same chemical shift in Fig. S10 [58]. Even though the ^{31}P MAS NMR resonance signal of anchored

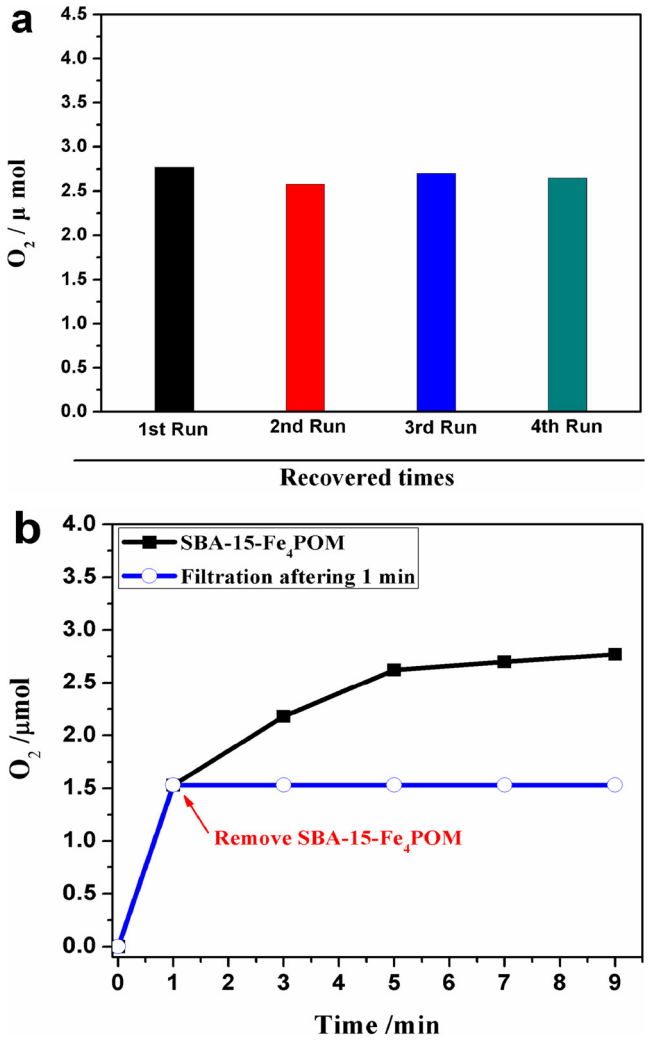

Fig. 9. (a) The evolution of O_2 in the photocatalytic heterogeneous system using fresh SBA-15-apts-Fe_4POM and recovered SBA-15-apts-Fe_4POM. (b) The evolution of O_2 in the photocatalytic system using fresh SBA-15-Fe_4POM and filtration the SBA-15-Fe_4POM after 1 min. Reaction conditions: $[Ru(bpy)_3]Cl_2$ (1.0 mM) and $Na_2S_2O_8$ (5.0 mM) and SBA-15-apts-Fe_4POM (10 mg) under photoirradiation (LED lamp, $\lambda \geq 420$ nm) at room temperature.

Fe_4POM after immobilization is weaker than that of fresh pure Fe_4POM, the unchanged chemical shift value certainly supports the identical eigenstructure $[P_2W_{15}O_{56}]^{12-}$ in polyoxometalate, indicating the effective heterogenization of robust Fe_4POM on the supported SBA-15 is constructed.

After the polyanion Fe_4POM is anchored on the surface of mesoporous SBA-15, the composite shows good stable under photocatalytic water oxidation conditions. Firstly, the molar ratio of Fe, P, W elements maintain essentially the same value between fresh and recycled SBA-15-apts-Fe_4POM in the EDX spectra, demonstrating the structure of Fe_4POM maintained intact (Fig. S11g, h). Secondly, no decomposition of Fe_4POM is detected by solid ^{31}P MAS NMR after photocatalytic water oxidation (Fig. 8), in which the chemical shift and comparative peak intensity maintain nearly the same to prove the stability of SBA-15-apts-Fe_4POM. Thirdly, structure characterization after the photocatalytic water oxidation by TEM and HRTEM (Fig. S11) indicates no change is found. Fourthly, to assess the chemical stability of SBA-15-apts-Fe_4POM in photochemical water oxidation, XPS characterization was conducted for the fresh and recovered composite catalyst. Those XPS spectra (Fig. S12) support the fact that structure of composite maintains integrity by the comparison of the almost same full scan, Fe 2p, W 4f, P 2p, Si 2p and O 1s spectra. Fifthly, through replenishing the same equivalent of $Na_2S_2O_8$ (5.0 mM), $Ru(bpy)_3Cl_2$ (1.0 mM) and recovered catalyst SBA-15-apts-Fe_4POM into fresh 80 mM borate buffer (pH = 9.0) solution, a nearly identical O_2 yield is achieved even for the fourth run compared with the first one (Fig. 9a). Sixthly, the oxygen evolution reaction stops immediately when the catalyst SBA-15-apts-Fe_4POM is removed by filtration after 1 min (Fig. 9b). Seventhly, no significant Fe is detected in the filtrate by ICP-AES, revealing no dissociation or leaching of iron occurs for the composite catalyst, SBA-15-apts-Fe_4POM. From all above experiments, the stability of SBA-15-apts-Fe_4POM is confirmed under heterogeneous photocatalytic water oxidation conditions.

Recovery and reuse of molecular catalysts after photocatalytic water oxidation reaction are important for sustainable process management. For each system, the homogeneous catalysts are difficult to recover while heterogeneous catalysts are reusable since they can be easily separated from reaction system. Therefore, it is realistic and necessary to heterogenize the homogeneous molecular catalyst. The heterogenization of homogeneous catalysis is forecasted to be the industrialization tendency for water splitting (including the half reaction of water oxidation). At the same time, building the close relationship between homogeneous and heterogeneous process is an elegant way to efficiently bridge the gap between these two traditional disciplines.

4. Conclusions

In summary, a carbon-free, molecular tetrairon(III)-substituted polyoxotungstate $[Fe_4^{III}(H_2O)_2(P_2W_{15}O_{56})_2]^{12-}$ can function in both homogeneous and heterogeneous modes for photo-driven catalytic water oxidation. This maximally earth-abundant POM, Fe_4POM catalyzes visible-light-driven oxygen evolution (O_2 yield of 48%, $TOF_{catalyst}$ of 5 s^{-1}, $TON_{catalyst}$ of 900 and Φ_{QY} yield of 24%) in solution and maintains its stability when anchored in apts-modified mesoporous SBA-15. It is the first time that homogeneous Fe_4POM was anchored on the surface of apts-modified mesoporous SBA-15 by the electrostatic interaction strategy (cation exchange). Solid-state ^{31}P NMR, XPS and TEM collectively establish that Fe_4POM remains intact before and after the photocatalytic water oxidation. The obtained heterogeneous SBA-15-apts-Fe_4POM performs good stability for the photocatalytic water oxidation, which could be recovered easily and recycled many times without activity loss. This research will provide insightful guidelines for designing rationally assembled immobilization of homogeneous robust POM catalysts on the mesoporous supporter, revealing the great potential application in recyclable photocatalytic water oxidation in heterogenization system.

Conflict of interest

The authors declare no competing financial interest.

Acknowledgements

This work was financially supported by the National Natural Science Foundation of China (Grants Nos. 21173105 and 21773096), Fundamental Research Funds for the Central Universities (lzujbky–2018–k08) and Natural Science Foundation of Gansu (17JR5RA186). We gratefully thank Prof. Craig L. Hill for his valuable discussions and English writing improvement and Prof. Junwei Zhao for his X-ray crystallography analysis.

Appendix A. Supplementary data

Supplementary material related to this article can be found, in the online version, at doi:https://doi.org/10.1016/j.apcatb.2018.07.014.

References

[1] N.S. Lewis, D.G. Nocera, Proc. Natl. Acad. Sci. 103 (2006) 15729–15735.

[2] R.E. Blankenship, D.M. Tiede, J. Barber, G.W. Brudvig, G. Fleming, M. Ghirardi, M.R. Gunner, W. Junge, D.M. Kramer, A. Melis, T.A. Moore, C.C. Moser, D.G. Nocera, A.J. Nozik, D.R. Ort, W.W. Parson, R.C. Prince, R.T. Sayre, Science 332 (2011) 805–809.
[3] Y. Shang, X. Chen, W. Liu, P. Tan, H. Chen, L. Wu, C. Ma, X. Xiong, J. Pan, Appl. Catal. B–Environ. 204 (2017) 78–88.
[4] A.J. Bard, M.A. Fox, Acc. Chem. Res. 28 (1995) 141–145.
[5] I. Dincer, Renew. Sustain. Energy Rev. 4 (2000) 157–175.
[6] N. Armaroli, V. Balzani, Angew. Chem. Int. Ed. 46 (2007) 52–66.
[7] H.B. Gray, Nat. Chem. 1 (2009) 7–7.
[8] Y. Tachibana, L. Vayssieres, J.R. Durrant, Nat. Photon. 6 (2012) 511–518.
[9] A. Kudo, Y. Miseki, Chem. Soc. Rev. 38 (2009) 253–278.
[10] Z. Han, F. Qiu, R. Eisenberg, P.L. Holland, T.D. Krauss, Science 338 (2012) 1321–1324.
[11] R. Shi, H. Ye, F. Liang, Z. Wang, K. Li, Y. Weng, Z. Lin, W. Fu, C. Che, Y. Chen, Adv. Mater. 30 (2018) 1705941.
[12] S. Cao, C. Wang, W. Fu, Y. Chen, ChemSusChem 10 (2017) 4306–4323.
[13] D. Zhong, W. Liu, P. Tan, A. Zhu, Y. Liu, X. Xiong, J. Pan, Appl. Catal. B–Environ. 227 (2018) 1–12.
[14] M. Graetzel, Acc. Chem. Res. 14 (1981) 376–384.
[15] J. Barber, Chem. Soc. Rev. 38 (2009) 185–196.
[16] L. Duan, L. Wang, F. Li, F. Li, L. Sun, Acc. Chem. Res. 48 (2015) 2084–2096.
[17] L. Yu, J. Lin, M. Zheng, M. Chen, Y. Ding, Chem. Commun. 54 (2018) 354–357.
[18] A. Sartorel, M. Carraro, G. Scorrano, R.D. Zorzi, S. Geremia, N.D. McDaniel, S. Bernhard, M. Bonchio, J. Am. Chem. Soc. 130 (2008) 5006–5007.
[19] Y.V. Geletii, Z. Huang, Y. Hou, D.G. Musaev, T. Lian, C.L. Hill, J. Am. Chem. Soc. 131 (2009) 7522–7523.
[20] Q. Yin, J.M. Tan, C. Besson, Y.V. Geletii, D.G. Musaev, A.E. Kuznetsov, Z. Luo, K.I. Hardcastle, C.L. Hill, Science 328 (2010) 342–345.
[21] Z. Huang, Z. Luo, Y.V. Geletii, J.W. Vickers, Q. Yin, D. Wu, Y. Hou, Y. Ding, J. Song, D.G. Musaev, J. Am. Chem. Soc. 133 (2011) 2068–2071.
[22] F. Song, Y. Ding, B. Ma, C. Wang, Q. Wang, X. Du, S. Fu, J. Song, Energy Environ. Sci. 6 (2013) 1170–1184.
[23] Q. Han, Y. Ding, Dalton Trans. 47 (2018) 8180–8188.
[24] H. Lv, Y.V. Geletii, C. Zhao, J.W. Vickers, G. Zhu, Z. Luo, J. Song, T. Lian, D.G. Musaev, C.L. Hill, Chem. Soc. Rev. 41 (2012) 7572–7589.
[25] J. Lin, Q. Han, Y. Ding, Chem. Rec. (2018), https://doi.org/10.1002/tcr.201800029.
[26] X.-B. Han, Z.-M. Zhang, T. Zhang, Y.-G. Li, W. Lin, W. You, Z.-M. Su, E.-B. Wang, J. Am. Chem. Soc. 136 (2014) 5359–5366.
[27] L. Yu, X. Du, Y. Ding, H. Chen, P. Zhou, Chem. Commun. 51 (2015) 17443–17446.
[28] B. Schwarz, J. Forster, M.K. Goetz, D. Yücel, C. Berger, T. Jacob, C. Streb, Angew. Chem. Int. Ed. 55 (2016) 6329–6333.
[29] L. Yu, Y. Ding, M. Zheng, H. Chen, J. Zhao, Chem. Commun. 52 (2016) 14494–14497.
[30] L. Yu, Y. Ding, M. Zheng, Appl. Catal. B–Environ. 209 (2017) 45–52.
[31] X. Du, Y. Ding, F. Song, B. Ma, J. Zhao, J. Song, Chem. Commun. 51 (2015) 13925–13928.
[32] R.G. Finke, M.W. Droege, P.J. Domaille, Inorg. Chem. 26 (1987) 3886–3896.
[33] R. Contant, W.G. Klemperer, O. Yaghi, Inorg. Synth. 27 (2007) 104–111.
[34] D. Zhao, J. Feng, Q. Huo, N. Melosh, G.H. Fredrickson, B.F. Chmelka, G.D. Stucky, Science 279 (1998) 548–552.
[35] L. Chen, K. Zhu, L.-H. Bi, A. Suchopar, M. Reicke, G. Mathys, H. Jaensch, U. Kortz, R.M. Richards, Inorg. Chem. 46 (2007) 8457–8459.
[36] X. Zhang, Q. Chen, D.C. Duncan, C.F. Campana, C.L. Hill, Inorg. Chem. 36 (1997) 4208–4215.
[37] S.J. Roosendaal, B. van Asselen, J.W. Elsenaar, A.M. Vredenberg, F.H.P.M. Habraken, Surf. Sci. 442 (1999) 329–337.
[38] T. Yamashita, P. Hayes, Appl. Surf. Sci. 254 (2008) 2441–2449.
[39] Y. Feng, J. Wei, Y. Ding, J. Phys. Chem. C 120 (2016) 517–526.
[40] J. Park, S. Ryu, M.-s. Han, S.J. Oh, Phys. Rev. B 37 (1988) 10867–10875.
[41] H. Li, F. Li, B. Zhang, X. Zhou, F. Yu, L. Sun, J. Am. Chem. Soc. 137 (2015) 4332–4335.
[42] M. Zheng, Y. Ding, L. Yu, X. Du, Y. Zhao, Adv. Funct. Mater. 27 (2017) 1605846.
[43] J. Wei, Y. Feng, P. Zhou, Y. Liu, J. Xu, R. Xiang, Y. Ding, C. Zhao, L. Fan, C. Hu, ChemSusChem 8 (2015) 2630–2634.
[44] M. Orlandi, R. Argazzi, A. Sartorel, M. Carraro, G. Scorrano, M. Bonchio, F. Scandola, Chem. Commun. 46 (2010) 3152–3154.
[45] R. Al-Oweini, A. Sartorel, B.S. Bassil, M. Natali, S. Berardi, F. Scandola, U. Kortz, M. Bonchio, Angew. Chem. Int. Ed. 53 (2014) 11182–11185.
[46] M.P. Santoni, G. La Ganga, V.M. Nardo, M. Natali, F. Puntoriero, F. Scandola, S. Campagna, J. Am. Chem. Soc. 136 (2014) 8189–8192.
[47] T. Yamase, Chem. Rev. 98 (1998) 307–326.
[48] S. Li, S. Liu, S. Liu, Y. Liu, Q. Tang, Z. Shi, S. Ouyang, J. Ye, J. Am. Chem. Soc. 134 (2012) 19716–19721.
[49] X.B. Han, Y.G. Li, Z.M. Zhang, H.Q. Tan, Y. Lu, E.B. Wang, J. Am. Chem. Soc. 137 (2015) 5486–5493.
[50] S.M. Lauinger, J.M. Sumliner, Q. Yin, Z. Xu, G. Liang, E.N. Glass, T. Lian, C.L. Hill, Chem. Mater. 27 (2015) 5886–5891.
[51] P. Shah, A.V. Ramaswamy, K. Lazar, V. Ramaswamy, Appl. Catal. A–Gen. 273 (2004) 239–248.
[52] A.C.C. Chang, S.S.C. Chuang, M. Gray, Y. Soong, Energy Fuel 17 (2003) 468–473.
[53] B. Erdem, R.A. Hunsicker, G.W. Simmons, E.D. Sudol, V.L. Dimonie, M.S. El-Aasser, Langmuir 17 (2001) 2664–2669.
[54] S.W. Knipe, J.R. Mycroft, A.R. Pratt, H.W. Nesbitt, G.M. Bancroff, Geochim. Cosmochim. Acta 59 (1995) 1079–1090.
[55] D.L. Legrand, H.W. Nesbitt, G.M. Bancroft, Am. Mineral. 83 (1998) 1256–1265.
[56] D. Pérez-Quintanilla, A. Sánchez, I. del Hierro, M. Fajardo, I. Sierra, J. Colloid Interface Sci. 313 (2007) 551–562.
[57] Y. Liu, Z. Liu, J. Gao, J. Dai, J. Han, Y. Wang, J. Xie, Y. Yan, J. Hazard. Mater. 186 (2011) 197–205.
[58] A. Indra, A. Acharjya, P.W. Menezes, C. Merschjann, D. Hollmann, M. Schwarze, M. Aktas, A. Friedrich, S. Lochbrunner, A. Thomas, M. Driess, Angew. Chem. Int. Ed. 129 (2017) 1675–1679.